DR BIN TANG (Orcid ID : 0000-0002-3851-2330)

Article type : Article

Structure and Microwave Dielectric Properties of the $Li_{2/3(1-x)}Sn_{1/3(1-x)}Mg_xO$ Systems (x=0 to 4/7)

ZIXUAN FANG[1,2] BIN TANG[1,2,*] YING YUAN [1,2] XING ZHANG[1,2]
SHUREN ZHANG[1,2]

1. National Engineering Center of Electromagnetic Radiation Control Materials,
University of Electronic Science and Technology of China, Jianshe Road, Chengdu 610054, P.R. China
2. State Key Laboratory of Electronic Thin Films and Integrated Devices,
University of Electronic Science and Technology of China, Jianshe Road, Chengdu 610054, P.R. China
*corresponding author: tangbin@uestc.edu.cn

Abstract

In this paper, the $Li_{2/3(1-x)}Sn_{1/3(1-x)}Mg_xO$ (LSMxO) ceramic systems were prepared by solid-state reaction using novel atmosphere-controlled sintering (x=0 to 4/7). Pure Li_2SnO_3 was observed for x=0, the $Li_2Mg_3SnO_6$ and Li_2SnO_3 coexisted for x=1/7, and the coexistence of three kinds of phases was detected for x=1/5 and 1/4, including $Li_4MgSn_2O_7$ impurity phase. Pure $Li_2Mg_3SnO_6$-like phase with cubic rock salt structure in Fm-3m space group was obtained in the range of 1/3~4/7. All samples showed well-dense and smooth microstructures. The microwave dielectric properties highly depended on the phase composition, bond valence, FWHM of Raman spectrum, Raman shift, average grain sizes and octahedral distortion. The LSMxO ceramics sintered at 1250 °C for 5 h possessed excellent comprehensive properties of ε_r= 15.43, $Q\times f$= 80,902 GHz and τ_f= +5.61 ppm/°C for x= 1/7. Typically, the LSMxO ceramics sintered at 1350 °C for 5 h showed a maximum $Q\times f$ of 168,330 GHz for x= 1/2.

Keywords: Microwave Dielectrics Ceramics; Microstructures; crystal structures;

1. Introduction

Microwave dielectric ceramics have played a paramount role as key components in the microwave devices ranging from any hand-held terminals to base stations due to the rapid growth in wireless communication industry [1]. To meet the specific request of fifth-generation (5G) communication and applications, these ceramic systems are required to possess the adjustable dielectric constant (ε_r), high quality factor ($Q\times f$) and near-zero temperature coefficient of the resonant frequency (τ_f) [2-4]. Great efforts have been made to explore the new ceramic systems, and study the correlation between structure and microwave dielectric characteristics.

In the past half-century, Li_2BO_3-MgO system (B=Ti, Sn), which is affiliated to the big family of rock salt structure phases, has drawn some attentions due to the phenomenon of order-disorder phase transition. In the case of Li_2TiO_3-MgO system, the substitution mechanism between Li/Ti and Mg has been confirmed by numerous literatures [5-13], which could be expressed as $2Li^{2+}+Ti^{4+}\leftrightarrow 3Mg^{2+}$. The substitution of Li/Ti for Mg leads to the ordered superstructure of Li_2TiO_3 phase transforming from a monoclinic structure in C2/c space group to a disordered cubic structure in Fm-3m space group. Two phase systems, Li_2TiO_3 ($0\leq x < 1/5$) and $Li_2Mg_3TiO_6$ ($1/5\leq x\leq 1/2$) phase, were found according to the formula of $Li_{2/3(1-x)}Ti_{1/3(1-x)}Mg_xO$ ($0\leq x\leq 1/2$). Recently, there are many investigations about the structures and microwave dielectric characteristics of $Li_{2/3(1-x)}Ti_{1/3(1-x)}Mg_xO$ systems, especially the ultra-low loss $Li_2Mg_3TiO_6$ (ε_r=15.2, $Q\times f$ =152,000 GHz, and τ_f= -39 ppm/°C). And the rock-salt structure $Li_2Mg_3TiO_6$ ceramics have been widely studied because of their excellent performance at microwave frequencies [9, 10].

In terms of Li_2SnO_3-MgO systems, however, there are just some fragmentary reports about their phase structure and microwave dielectric characteristics [14-16]. For example, Castellanos *et al.* revealed that Li_2SnO_3-MgO compound could form solid solution, and $Li_4MgSn_2O_7$ (L4MS2) could exist as an equilibrium phase [14]. Fu *et al*. reported the excellent microwave dielectric properties of $Li_2Mg_3SnO_6$ phase [10] and claimed that Li_2SnO_3 ceramics co-doped with MgO–LiF could eventually form the $Li_2Mg_3SnO_6$ phase [15]. Moreover, according to the solid solution theory[17], the cation sizes of Li_2SnO_3 and MgO were very similar; the ionic radii of the cations were R(Mg^{2+})=0.72 Å and R[average (Li, Sn)]=0.737 Å [18]. The difference (ΔR) between R(Mg^{2+}) and R[average (Li, Sn)]=0.737 Å was calculated as 2.3%, which was much less than 15%. Thus, MgO and Li_2SnO_3 were able to form solid solutions. Similar to Li_2TiO_3-MgO system, it was likely that $Li_{2/3(1-x)}Sn_{1/3(1-x)}Mg_xO$ solid-solutions would exist in the range of 0~4/7, and the $Li_2Mg_3SnO_6$ phase should belong to the $Li_{2/3(1-x)}Sn_{1/3(1-x)}Mg_xO$ systems. On the basis of previous discussion, we deduced that the formula of $Li_{2/3(1-x)}Sn_{1/3(1-x)}Mg_xO$ could also be written as $Li_2Mg_{3+y}SnO_{3+y}$ (y=0~4), where the x equals $y/(3+y)$. The corresponding relationships between $Li_{2/3(1-x)}Sn_{1/3(1-x)}Mg_xO$ and $Li_2Mg_{3+y}SnO_{3+y}$ are summarized as follows: $Li_{2/3}Sn_{1/3}O$ (Li_2SnO_3(LS)), $Li_{4/7}Sn_{2/7}Mg_{1/7}O$ ($Li_2Mg_{0.5}SnO_{3.5}$), $Li_{8/15}Sn_{4/15}Mg_{1/5}O$ ($Li_2Mg_{0.75}SnO_{3.75}$), $Li_{1/2}Sn_{1/4}Mg_{1/4}O$ (Li_2MgSnO_4), $Li_{4/9}Sn_{2/9}Mg_{1/3}O$ ($Li_2Mg_{1.5}SnO_{4.5}$), $Li_{2/5}Sn_{1/5}Mg_{2/5}O$ ($Li_2Mg_2SnO_5$), $Li_{4/11}Sn_{2/11}Mg_{5/11}O$ ($Li_2Mg_{2.5}SnO_{5.5}$), $Li_{1/3}Sn_{1/6}Mg_{1/2}O$ ($Li_2Mg_3SnO_6$(L2M3S)) and $Li_{2/7}Sn_{1/7}Mg_{4/7}O$ ($Li_2Mg_4SnO_7$), respectively.

In our current work, all samples contained certain amounts of lithium elements. It is common that lithium contents will seriously volatilize in lithium containing materials when samples are sintered under high temperature circumstances (Refer to attached supplementary Fig. 1 and Fig. 2) [7, 10, 11, 19]. And the porous microstructure caused by the loss of Li element will seriously deteriorate the microwave dielectric properties, which also is detrimental for LSMxO to be practically used in the microwave circuits. Thus, we adopted the chemical stable ZrO_2 powders as the protective material for the $Li_{2/3(1-x)}Sn_{1/3(1-x)}Mg_xO$ (0~4/7) pellets to be buried in and Li_2CO_3 powders were used to provide Li-rich sintering atmosphere, which was a brand new sintering method for microwave ceramics. Moreover, in this investigation, the phase structures, crystal structures, sintering behaviors and microwave dielectric properties of $Li_{2/3(1-x)}Sn_{1/3(1-x)}Mg_xO$ (0~4/7) ceramics were investigated by

XRD, Rietveld refinement method, Raman scattering theory, SEM, EDX, and bond valence theory using a novel atmosphere-controlled sintering.

2. Experimental procedure

In this work, three kinds of raw materials with at least 99.5 % purity were used to synthesize the $Li_{2/3(1-x)}Sn_{(1-x)}Mg_xO$ samples using the conventional solid-state method. The raw powders, $(Mg(OH)_2 \cdot 4MgCO_3 \cdot 5H_2O$ (Xiantao ZhongXing Electric Co., Ltd, Xiantao, China), Li_2CO_3 (Chengdu Kelong Chemical Co., Ltd, Chengdu, China) and SnO_2 (Mianyang Yuanda New Materials Co., Ltd, Mianyang, China), were weighed according to the formula of $Li_{2/3(1-x)}Sn_{(1-x)}Mg_xO$ (LSMxO), where x =0, 1/7, 1/5, 1/4, 1/3, 2/5, 5/11, 1/2 and 4/7, and were ball milled in a nylon jar with zirconia balls in ethanol for 7 h. The resulting mixtures for x=0~4/7 were dried and fired at 900 °C for 4 h. Later, the calcined powders were reground for 5 h, dried, mixed with a 6 wt. % of a 10% solution of polyvinyl alcohol (PVA) as an organic binder and homogeneously granulated in an agate mortar and pestle. The obtained powder was axially pressed into cylindrical disks with a thickness of 7.5 mm and a diameter of 15 mm under a pressure of 200 MPa. After preparing the LSMxO disks, all samples were preheated at 600 °C for 2 h to remove the organic binder, later they were sintered from 1200 °C to 1400 °C for 5 h in controlled atmosphere with heating and cooling rate of 6 °C/min. Fig. 1 presents the schematic placement of samples for the novel atmosphere sintering. According to Fig. 1, the chemical stable ZrO_2 powders were used as the protective material for the LSMxO pellets to be buried in and Li_2CO_3 powders were used to provide Li-rich sintering atmosphere.

The apparent densities (ρ_{ap}) of the LSMxO ceramics were measured using the Archimedes' principle. The relative densities were calculated from the formula, $\rho_{rela} = \frac{\rho_{ap}}{\rho_{theo}} \times 100\%$. For x=1/7, the theoretical density of the LMxSO ceramics was calculated using the equation, $\rho_{\text{theo}} = \frac{\rho_1 v_1 + \rho_2 v_2}{v_1 + v_2}$, where v_1 and v_1 were the volume percentage of $Li_2SnO_3$and $Li_2Mg_3SnO_6$ with densities ρ_1 and ρ_2, respectively. And for x=0 and 1/3≤x≤4/7, the theoretical density of the LMxSO ceramics was calculated using the equation, $\rho_{theo} = \frac{nA}{VN_A}$, where n was the number of atoms associated with unit cell, A was the atomic weight, V was the volume of unit cell and N_A was the Avogadro's number. Powder phase compositions were examined by X-ray diffraction (XRD) using CuKα radiation (Philips x'pert Pro MPD, Netherlands), and the refined lattice parameters of samples were analyzed by GSAS suite with EXPGUI software , in which the reliability was evaluated by three factors (R_{wp}-reliability factor of weighted patterns, R_p-reliability factor of patterns, x^2-goodness of fit indicator). The visualization of crystal structure of LSMxO ceramics was obtained by VESTA software [20]. Scanning electron microscopy (SEM) and energy dispersive X-ray spectroscopy (EDX) (HITACHI S-9220, Japan) were employed to study the thermally etched surface photograph of the LSMxO ceramics. The average grain sizes of LSMxO for 1/3 ≤x ≤1/7 were determined from SEM micrographs using Image-Pro Plus software [21]. The Raman spectra were collected by inVia Raman Microscrope (RENISHAW, UK) and analyzed by professional Labspec5. The 514 nm line of He–Ne laser source with constant power was used as the exciting wavelength for LSMxO ceramics. The ε_r and $Q\times f$ values of polished samples at 8~12 GHz were collected by a network analyzer (Agilent Technologies E5071C, USA) using the Hakki–Coleman dielectric resonator method in TE011 mode and temperature chamber (DELTA 9023, Delta Design, USA). The τ_f was calculated from data obtained in the temperature range of 25~85 °C according to the equation: $\tau_f = (10^6\times\Delta f/f_{t1}\times\Delta T)$ (1), where f_{t1} is the resonant frequencies at the measuring temperature t_1 (25 °C).

3. Results and discussion

Fig. 2 displays the powder XRD patterns of the $Li_{2/3(1-x)}Sn_{1/3(1-x)}Mg_xO$ ceramic systems (x=0 to 4/7) sintered in controlled atmosphere at optimal temperatures for 5 h. For x=0, all characteristic peaks were identified as pure Li_2SnO_3 (JCPDS#31-0761) phase with monoclinic rock salt structure in C2/c space group, and the strongest peak of (002) correlated with the long range ordering (LRO) and preferred orientation of grain growth along the c axis was also observed [5, 15, 22]. With addition of 1/7 mol Mg contents, a secondary phase of $Li_2Mg_3SnO_6$ (JCPDS#

39-0932) was detected accompanied by a reduction of $\mathrm{Li_2SnO_3}$ phase, and the intensity of (002) peak sharply decreased. This phenomena was in agreement with Keulen *et al*'s report of Li/Sn/Mg catalysts [16] and Fu *et al*'s investigation of $\mathrm{Li_2SnO_3}$ co-doped with MgO and LiF [15], which indicated the following chemical reaction happened: $\mathrm{Li_2SnO_3}\ (\mathrm{monoclinic\ (C2/c)}) + 3\mathrm{MgO}\ (\mathrm{cubic\ (Fm\bar{3}m)}) \rightarrow \mathrm{Li_2Mg_3SnO_6}\ (\mathrm{cubic\ (Fm\bar{3}m)})\ (2)$. XRD results demonstrated the existence of $\mathrm{Li_2Mg_3SnO_6}$ by the presence of $2\theta = 42.57^{\circ}$ characteristic peak and will be further evidenced by refinement of XRD and EDX analysis later. Meanwhile, our XRD results were different to the Castellanos's study [14] of phase diagram for the join $\mathrm{Li_2SnO_3}$-MgO system where only $\mathrm{Li_4MgSn_2O_7}$ or $\mathrm{Li_2SnO_3}$ existed in the range of $0 < x \leq 1/7$. For $1/5 \leq x \leq 1/4$, the mixture phases of $\mathrm{Li_4MgSn_2O_7}$ (JCPDS#37-1164), $\mathrm{Li_2Mg_3SnO_6}$ and $\mathrm{Li_2SnO_3}$ were observed, and intensity of $\mathrm{Li_4MgSn_2O_7}$ impurity phase and $\mathrm{Li_2Mg_3SnO_6}$ phase became stronger as x increased. However, with increasing x larger than 1/4 mol, it was remarkable that six characteristic peaks of all samples were indexed as (1, 1, 1), (2, 0, 0), (2, 2, 0), (3, 1, 1), (2, 2, 2) and (4, 0, 0), which was very similar to that of single $\mathrm{Li_2Mg_3SnO_6}$ phase with cubic rock salt structure in Fm-3m space group. Thus, the substitution of Li/Sn for Mg occurred, formed solid solutions, and the substitution reaction equation can be explained as $3\mathrm{MgO} \xrightarrow{\mathrm{Li_2SnO_3}} 2\mathrm{Mg}_{\mathrm{Li}}^{\cdot} + \mathrm{Mg}_{\mathrm{Sn}}^{\prime\prime} + 3\mathrm{O_o}(3)$. It was clear that as the Mg content increased ($1/3 \leq x \leq 4/7$), the six characteristic peaks were moving towards higher 2θ angles steadily, which indicated that there was shrinkage of cell volume and cell parameters according to the Bragg's Law (λ=2dsinθ) [23]. This finding was attributable to the smaller cations of Mg ($R(\mathrm{Mg^{2+}})$=0.72 Å) than the average the ionic radii of Li/Sn ($R[2/3\mathrm{Li^{+}}+1/3\mathrm{Sn^{4+}}]$=0.737 Å). It was necessary to analyze the fine XRD data of LSMxO ceramics by Rietveld refinement method to further confirm the exact phase compositions and crystal structure.

Because the indices of lattice planes, space group and crystal system of $\mathrm{Li_4MgSn_2O_7}$ phase were unknown, Rietveld refinement was just carried out on the fine XRD data for x=0, 1/7, 1/3, 2/5, 5/11, 1/2 and 4/7. Fig. 3 shows the representative plots of experimental (red circle) and calculated (blue line) X-ray diffraction for the

$Li_{2/3(1-x)}Sn_{1/3(1-x)}Mg_xO$ ceramic systems sintered at optimal temperatures for 5 h with (a) x=0, (b) x=1/7, (c) x=1/3 (d) x=2/5 (e) x=1/2 and (f) x=4/7. For x=0, the data were obtained using C2/c space group, and the sample was confirmed as pure Li_2SnO_3 phase and in monoclinic system (α=90º, β=100.341º, γ=90º). For x=1/7, the result of refined XRD data showed that the composite systems consisted of the Li_2SnO_3 (monoclinic (C2/c)) and $Li_2Mg_3SnO_6$ (cubic (Fm-3m)) phase. For x=1/3, 2/5, 5/11, 1/2 and 4/7, all samples were recognized as cubic rock salt structure in Fm-3m space group. Table 1 summarizes phase composition, crystal structure, lattice parameters, and unit cell volume of $Li_{2/3(1-x)}Sn_{1/3(1-x)}Mg_xO$ systems (x=0 to 4/7) ceramics sintered at optimal temperature by controlled atmosphere. It was clear that the refinement factors of R_{wp}, R_p, and x^2 for refined XRD were in the range of 2~7%, 1~6%, and 1~3, thus our structure models were established with high reliability. As shown in table 1, the cell volume decreased from 76.852 Å^3 at x=1/3 to 76.079 Å^3 at at x=4/7, which was in accordance to the analysis of XRD pattern. Fig. 4 also describes the representative schematic illustration of $Li_{2/3(1-x)}Sn_{1/3(1-x)}Mg_xO$ ceramics with typical rock-salt crystal structure for (a) monoclinic structure in C2/c space group (Li_2SnO_3) and (b) cubic structure in Fm-3m space group ($Li_2Mg_3SnO_6$). According to Fig. 4(a), the Li_2SnO_3 phase had a preferred orientation along the c axis and Li/Sn atoms occupied different positions. As illustrated in Fig. 4(b), the $Li_2Mg_3SnO_6$ phase showed a face-centred-cubic structure with extremely high symmetry, and it was similar to the structure of MgO with Li/Mg/Sn cations randomly distributed over the Mg^{2+} sites. According to the Wyckoff Positions of group 225 and refinement results, the Li/Mg/Sn cations were coordinated with six oxygen atoms where the Li/Mg/Sn cations held 4a Wyckoff positions and oxygen ions occupied 4b Wyckoff positions.

It is generally considered that Raman shift and the full-width-at-half maximum (FWHM) are closely correlated with the microwave dielectric characteristics, and the Raman spectra was utilized to better understand the relationship between crystal structures and microwave dielectric properties. Fig. 5 shows (a) Raman spectra of $Li_{2/3(1-x)}Sn_{1/3(1-x)}Mg_xO$ ceramic systems sintered at optimal temperatures in controlled atmosphere for 5 h and

(b) the amplified spectra of Raman shift in the region of 500~700 cm^{-1}. According to Denisova *et al.*'s investigation [24], the band at 590 cm^{-1} was considered to be Sn-O stretching vibration. The bands in the region of 366 and 239~320 cm^{-1} were associated with the Li-O stretching vibrations and O-Li-O bending vibrations, respectively. In the range of 0~1/4, the mode at 367 cm^{-1} gradually widened and weakened, which can be assigned with the decrease of cation ordering with increasing *x*. The broadening and weakening of modes at around 367 cm^{-1} for XRD was associated with long range disordering. The Sn-O stretching vibration mode at around 590 cm^{-1} weakened sharply, which can be ascribed to the decrease of Li_2SnO_3 phase with increasing *x* from 0 to 1/4. It was noticeable that a weak vibration mode at around 643 cm^{-1} was detected at *x*=1/7 for the first time. And the appearance of the new mode for XRD was correlated to the single Li/Sn/Mg-O vibration mode in $Li_2Mg_3SnO_6$ phase [15]. Although the $Li_4MgSn_2O_7$ phase was observed in XRD pattern for *x*=1/5 and 1/4, no special Raman peaks could be detected and some peaks at around 261 cm^{-1} and 317 cm^{-1} even disappeared. Because there was lack of basic crystal information for $Li_4MgSn_2O_7$ phase and it evolved from the Li_2SnO_3 phase, the possible explanation was that the $Li_4MgSn_2O_7$ phase presented the vibration modes similar to some of Li_2SnO_3 phase. Due to the high symmetry of crystals in Fm-3m space group [9], only one peak at around 643 cm^{-1} was found with increasing *x* from 1/3 to 4/7, implying that only one vibration mode existed in these samples. And the single peak was associated with pure $Li_2Mg_3SnO_6$ phase for XRD pattern, which was consistent with Wu. *et al*'s [9] and Fu *et al*'s studies[15]. It was remarkable that intensity of peaks at approximately 643 cm^{-1} enhanced greatly, indicating that the intensity of Li-O, Mg-O and Sn-O vibration mode became stronger with increasing Mg elements. Meanwhile, peaks at around 643 cm^{-1} had a blue shift from 641.7 cm^{-1} to 647.44 cm^{-1} in the range of 1/3~4/7. The blue shift was highly correlated to the decrease of cell volume from 76.852 $Å^3$ to 76.079 $Å^3$; a smaller cell volume was usually related to a higher energy to activate this local vibration mode [25]. Importantly, the FWHM of spectra using Gaussian fitting firstly decreased from 39.06 cm^{-1} at *x*=1/3 to 36.22 cm^{-1} at *x*=1/2, later increased to 40.76

cm^{-1} x=4/7.

Fig. 6 presents the SEM images of $Li_{2/3(1-x)}Sn_{1/3(1-x)}Mg_xO$ ceramic systems sintered at optimal temperatures for 5 h in controlled atmosphere with (a) x=0, (b) x=1/7, (c) x=1/5, (d) x=1/4 (e) x=1/3 (f) x=2/5 (g) x=5/11 (h) x=1/2 and (i) x=4/7. As shown in Fig. 6, all specimens demonstrated good grains and clear boundaries, and it was significant to find that for $1/3\leq x\leq 4/7$, samples showed an absolutely well-dense and smooth microstructure. It was also noted that micro-cracks or cleavages [11] caused by the phase transition or porosity in Li_2BO_3 (B=Ti, Sn, Zr) did not occur in our work, which may be related to the controlled atmosphere. This finding indicated the samples sintered in controlled atmosphere had much better growing surroundings than that reported in such many literatures [6, 10, 11], and we managed to “cure” the serious volatilization of lithium. The EDX was employed to study element compositions of marked grains (A~L), as shown in Fig. 6. The representative EDX spectrum of marked grains corresponding to Fig. 6 are presented in Fig. 7, and the collected data of EDX are listed in Table 2. According to Fig. 6(a), only bar-shaped grains were observed for x=0, and grain A showed only Sn and O elements. It was clear that these grains had a preferred orientation of grain growth, and they should be the Li_2SnO_3 phase. The coexistence of $Li_2Mg_3SnO_6$ and Li_2SnO_3 in specimens was observed by distinguishing from their EDX analysis for grain B and C in Fig. 6(b) and Table 2. According to Fig. 6(c)~(d) and the EDX analysis, three kinds of grains coexisted, the large abnormal grains D and F should be the $Li_4MgSn_2O_7$ phase, and the small polygon-shaped grains E and G were confirmed as Li_2MgSnO_6 phase. As shown in Fig. 6(e)~(i), only the polygon-shaped grains could be detected for $1/3\leq x\leq 4/7$, and with increasing x, the ratio of Mg: Sn almost increased from 1.5 to 4. Fu *et al.* also revealed that the Li_2MgSnO_6-like phase presented a polygon-shaped grain [15].Thus, the grains H~L should be considered as Li_2MgSnO_6-like phase. At the same time, it was recognizable that the average grain sizes steadily increased from 5.313 um at x=1/3 to 9.126 um at x=1/2, but decreased to 6.148 um at x=4/7. Furthermore, a high densification was achieved, and the homogeneous microstructure was obtained at x=1/2.

The relative densities were calculated to better understand the densification process, and because of the lack of basic crystal information for $Li_4MgSn_2O_7$ phase, relative densities were just calculated for x=0, 1/7, and 1/3~4/7. Fig. 8 illustrates the relative density (x=0, 1/7, and 1/3~4/7) of ceramics sintered by controlled atmosphere at 1200~1400 °C for 5 h. As shown in Fig. 8, all specimens demonstrated good relative densities higher than 95.5% although some pores could be seen in Fig. 6(a), which was attributable to the good growing surroundings provided by controlled atmosphere. It was apparent that in the range of 0~1/7, the relative density was improved because of the elimination of pores seen in Fig. 6(a)~(b). For $1/3\leq x\leq 1/2$, the optimal relative density gradually increased, and reached a saturated value of 98.8% at x=1/2. The relative density is usually affected by cell volume, pores and microstructure. Thus, the decrease of cell volume was beneficial to the improvement of relative density in the region of 1/3~1/2. Furthermore, because the microstructure became more homogeneous accompanied by the increase of average grain sizes, the relative density was significantly improved to a large value of 98.8% at x=1/2. However, when extra Mg contents were added (x=4/7), the microstructure become inhomogeneous and the average grain sizes decreased, leading to the decrease of relative density [26, 27].

Fig. 9(a) shows the dielectric constant of LSMxO ceramic systems (x=0~4/7) sintered by controlled atmosphere at 1200~1400 °C for 5 h. It is generally considered that dielectric constant is strongly affected by relative density, phase compositions, dielectric polarizability, bond valence and Raman shift. With increasing x from 0 to 1/7, the optimal ε_r value slightly decreased from 16.7 to 15.4 because of the appearance of $Li_2Mg_3SnO_6$ phase (ε_r=12.7).The abrupt decrease in dielectric constant from 14.2 to 11.7 as $1/5\leq x\leq 1/4$ should be ascribed to the substantially increase in $Li_4MgSn_2O_7$ impurity phase. For $1/3\leq x\leq 4/7$, the variation of dielectric polarizability and Raman shift should be responsible for the dielectric constant due to the single $Li_2Mg_3SnO_6$-like phase and high relative density (96%$<x$). We calculated the theoretical dielectric constant of $Li_{2/3(1-x)}Sn_{1/3(1-x)}Mg_xO$ in the region of 1/3~4/7 using the Clausius–Mossotti equation, $\varepsilon_{theo} = \frac{3}{1-\frac{b\alpha_m}{V_m}} - 2$ (4), where the ε_{theo} is the theoretical dielectric constant, V_m is the mole volume, b equals 4π/3 and the α_m is the molecular polarizability. The α_m can be obtained according to additive rules [18] using the following formula, $\alpha[(Li_{2/3}Sn_{1/3})_{1-x}Mg_xO]=[2/3\alpha(Li^+)+1/3\alpha(Sn^{4+})](1-x)+x\times\alpha(Mg^{2+})+\alpha(O^{2+})=3.735-0.423x$ (5). The molecular polarizability decreased with increasing x value. Fig. 9(b) displays the variation of ε_{theo} and optimal ε_r versus the x value in the region of 1/3~4/7. It was clear that both of the ε_{theo} and ε_r values monotonously decreased with increasing Mg contents. The ε_r was higher than ε_{theo} and the deviations of ε_r from ε_{theo} also decreased, which could be explained by the bond valence theory [28] with increasing x. The bond valence of Li-O, Sn-O and Mg-O were based on the equation, $V_i = \sum_{i=1}^{n=j} v_{ij}$ (6), and $v_{ij} = \exp(\frac{R_{ij}-d_{ij}}{b'})$(7) where R_{ij} is the bond valence parameter, d_{ij} is the length of a bond between atom i and j, and b' is commonly considered to be 0.37 Å. Table 3 contains the bond valence (V_{bv}) of $Li_{2/3(1-x)}Sn_{1/3(1-x)}Mg_xO$ systems for $1/3 \leq x \leq 4/7$, and Table 4 summarizes The theoretical dielectric polarizability (α_m), theoretical dielectric constant (ε_{theo}) and observed (ε_r) of $Li_{2/3(1-x)}Sn_{1/3(1-x)}Mg_xO$ systems for these samples. It was remarkable that three kinds of bond valence ($V_{Li\text{-}O}$, $V_{Mg\text{-}O}$ and $V_{Sn\text{-}O}$) had different degrees of improvement. And a lager bond valence ($V_{Li\text{-}O}$, $V_{Mg\text{-}O}$ and $V_{Sn\text{-}O}$) indicated that the bond strength between oxygen and Li/Mg/Sn-site ion was stronger, resulting in the decrease of rattling effect of Li/Mg/Sn-sites for LSMxO ceramics [29]. Thus, the deviations of ε_r from ε_{theo} decreased sharply from 15.74% to 2.82%. Fig. 9(c) presents the relationship between Raman shift and ε_r versus the x value. It clearly indicated that the change of Raman shift was inverse to that of ε_r. This was related to the rigidity of the oxygen octahedral; the smaller cell volume implied the rigidity of the oxygen octahedral [30]. This result also clearly indicated that the rigid oxygen octahedra was associated with low dielectric constant.

The $Q\times f$ values of LSMxO ceramic systems (x=0~4/7) sintered at 1200~1400 °C by controlled atmosphere for 5 h are plotted in Fig. 10(a). The $Q\times f$ values were highly dependent on the Mg contents. For the microwave dielectric materials, the dielectric loss are usually influenced by the relative density, secondary phase, packing fraction, the FWHM of vibration modes and grain sizes [31, 32]. As shown in Fig 10(a), there was a slight increase of $Q\times f$ value from 56,747 GHz at x=0 to 80,902 GHz at x=1/7 due to the formation of $Li_2Mg_3SnO_6$ phase ($Q\times f$= 168,330) and improvement of relative density. Later, however, further increase in Mg contents (x=1/4) seriously deteriorated the $Q\times f$ value to 55,473 GHz due to the increase in $Li_4MgSn_2O_7$ impurity phase. In the region of $1/3 \leq x \leq 4/7$, all samples presented high $Q\times f$ value, and the optimal $Q\times f$ was improved from 105,084 GHz at x=1/3 to the maximum value of 168,330 GHz at x=1/2, but it went down to 125,864 GHz x= 4/7. Because the single phase and high relative densities were obtained for LSMxO ceramics, packing fraction, the FWHM of vibration modes and grain sizes should be comprehensively taken into consideration to discuss the variation of $Q\times f$ values. The packing fraction were calculated according to the equation, $\text{Packing fraction (\%)} = \frac{volume\ of\ packed\ ions}{volume\ of\ the\ primitive\ unit\ cell}$ (8). And the Packing fraction data were collected in Table 2. It clearly indicated that the Packing fraction increased sharply increase from 39.93 % at x=1/3 to 53.47% at x=1/2, leading to the improvement of $Q\times f$ values to some extent. But the $Q\times f$ value did not correspondingly increase with the further enhancement of Packing fraction up to 62.63% at x=4/7. As reported by Chen *et al* [30], the quality factors of microwave ceramics were strongly influenced by FWHM of vibration modes, and the change of FWHM for peaks at around 643 cm^{-1} should contribute to the variation of $Q\times f$ since only one vibration mode was observed in this range. Fig. 10(b) describes the function of FWHM and optimal $Q\times f$ versus the x value. The quality factor is inversely proportional to the FWHM, which was highly consistent with such many reports about the researches of damping characters for microwave propagation in microwave dielectric ceramics [30, 33, 34]. Fig. 10(c) illustrates the variation of average grain size and optimal $Q\times f$ versus the x value. It was remarkable that the change of $Q\times f$ was similar to the variation of average grain sizes. The average grain sizes had significant effects on $Q\times f$ values because larger grain sizes reduced the number of grain boundaries per unit volume, resulting in lower dielectric loss [35]. As a result, the FWHM of Raman peaks and average grain sizes were mainly attributable to the change of $Q\times f$ values. And Table 5 provided the exact peak position and corresponding FWHM of Raman spectra at around 643 cm^{-1} versus cell volume (V), optimal $Q\times f$ and average grain sizes for $Li_{2/3(1-x)}Sn_{1/3(1-x)}Mg_xO$ systems sintered at optimal temperature by controlled atmosphere with $1/3 \leq x \leq 4/7$**.**

Fig. 11 (a) presents the temperature coefficient of the resonant frequency (τ_f) of LSMxO (x=0~4/7) sintered at optimal temperatures by controlled atmosphere for 5 h. The τ_f value monotonously changed from positive value of 24.8 ppm/°C at x=0 into negative value of -37.3 ppm/°C with increasing Mg contents, and it was significant that the near-zero τ_f value (5.61 ppm/°C) could be obtained at x=1/7. It is generally considered that the τ_f value shows a high dependence on the phase composition, octahedral distortion (δ) and bond valence (V_{bv}) [29, 36-38]. For $0 \leq x \leq 1/4$, the appearance of $Li_2Mg_3SnO_6$ phase (τ_f=-27.4 ppm/°C) and $Li_4MgSn_2O_7$ impurity phase should be responsible for the steady decreasing τ_f. In the range of 1/3~4/7, because only the $Li_2Mg_3SnO_6$-like phase was observed, the variation of δ and V_{bv} should mainly be considered to influence the changing τ_f value. And the octahedral distortion was calculated using $\delta = \frac{(\text{B−O distance}_{largest})-(\text{B−O distance}_{smallest})}{\text{B−O distance}_{average}}$ (9). Function of octahedral distortion and τ_f versus the x value is plotted in Fig 11(b), and Table 3 provides the corresponding data of octahedral distortion (δ). With increasing Mg content, the octahedral distortion increased, thereafter the τ_f decreased. This result was agreed with the investigations that temperature coefficient of dielectric constant (τ_ε) increased with the tilting of oxygen octahedral in the peroviske compound [29, 39], which corresponded to the decrease of τ_f. Fig. 11(c) displays the variation of $V_{Li/Mg/Sn-O}$ and optimal τ_f versus the x value in the region of 1/3~4/7. As we can see, the τ_f decreased with the enhancement of V_{Li-O}, V_{Mg-O}, and V_{Sn-O}.

In summary, we employed a new method of atmosphere-controlled sintering to prepare the

$Li_{2/3(1-x)}Sn_{1/3(1-x)}Mg_xO$ ceramic systems (x=0 to 4/7), leading to the solving of serious lithium volatilization in lithium containing ceramics. With the increasing Mg content in LSMxO, the adjustable microwave dielectric properties were obtained. It was significant that the LSMxO ceramics sintered in controlled atmosphere at 1250 °C for 5 h possessed excellent comprehensive properties of ε_r= 15.43, $Q\times f$= 80,902 GHz and τ_f= +5.61 ppm/°C for x= 1/7. And the LSMxO ceramics sintered in controlled atmosphere at 1350 °C for 5 h showed an maximum $Q\times f$ value of 168,330 GHz for x= 1/2. Furthermore, the LSMxO ceramics exhibited a wide sintering temperature range from 1225 °C to 1375 °C, which was promising to be used in the commercial devices.

4. Conclusions

In this paper, the $Li_{2/3(1-x)}Sn_{1/3(1-x)}Mg_xO$ ceramic systems were prepared by solid-state reaction method using novel atmosphere-controlled sintering (x=0 to 4/7). The correlations between phase composition, crystal structures and microwave dielectric properties of LSMxO systems were analyzed systematically and based on the comprehensive utilization of XRD, Rietveld refinement method, Raman scattering theory, SEM, EDX, and bond valence theory. According to results of XRD, Raman spectrum, Rietveld refinement, SEM and the EDX analysis, the pure Li_2SnO_3 phase with preferred orientation of grain growth was observed for x=0. The small polygon-shaped $Li_2Mg_3SnO_6$ and bar-shaped Li_2SnO_3 in specimens coexisted for x=1/7. The coexistence of three kinds of grains was detected for x=1/5 and 1/4, in which the large abnormal grains were confirmed as $Li_4MgSn_2O_7$ phase. In the range of 1/3~4/7, pure $Li_2Mg_3SnO_6$-like phase with cubic rock salt structure in Fm-3m space group was obtained for these samples. All specimens demonstrated good grains and clear boundaries, and it was significant to find that samples showed well-dense and smooth microstructures. The microwave dielectric properties of LSMxO systems highly depended on the phase composition, dielectric polarization, bond valence, FWHM of Raman spectrum, Raman shift, packing fraction, average grain sizes and octahedral distortion. The ε_r values of 9.98~16.9, $Q\times f$ values of 56,747~168,330 GHz and τ_f of -37.3 to +24.8 ppm/°C were observed in whole substitution range. It was significant that the LSMxO ceramics sintered in controlled atmosphere at 1250 °C for 5 h possessed excellent comprehensive properties of ε_r= 15.43, $Q\times f$= 80,902 GHz and τ_f= +5.61 ppm/°C for x= 1/7. Typically, the LSMxO ceramics sintered in controlled atmosphere at 1350 °C for 5 h showed an maximum $Q\times f$ value of 168,330 GHz accompanied by ε_r of 12.7 and τ_f of -27.4 ppm/°C for x= 1/2.

Acknowledgements

This work was supported by National Natural Science Foundation of China (Grant No. 51402039 and 51672038) and by the Open Foundation of National Engineering Research Center of Electromagnetic Radiation Control Materials (ZYGX2016K003-5). Zixuan Fang gratefully acknowledged support from the China Scholarship Council (CSC, 201706070025) during a visiting study at the University of California, Berkeley.

References

[1] Reaney, IM. Iddles D. Microwave Dielectric Ceramics for Resonators and Filters in Mobile Phone Networks. *J. Am. Ceram. Soc*. 2006;89:2063-2072.

[2] Osseiran, A. Boccardi F. Braun V, et al. Scenarios for 5G mobile and wireless communications: the vision of the METIS project. *IEEE. Commun. Mag*. 2014;52:26-35.

[3] Sebastian, MT. Ubic R. Jantunen H. *Microwave Materials and Applications*. 1st ed. New York, USA: John Wiley & Sons, 2017.

[4] Sebastian, MT. *Dielectric materials for wireless communication*. 1st ed. Oxford, UK: Elsevier; 2010.

[5] Castellanos, M. West AR. Order-disorder phenomena in oxides with rock salt structures: the system Li_2TiO_3-MgO. *J. Mater. Sci.* 1979;14:450-454.

[6] Bian, JJ. Dong YF. New high Q microwave dielectric ceramics with rock salt structures: $(1-x)Li_2TiO_3 + x$MgO system ($0 \le x \le 0.5$). *J. Eur. Ceram. Soc*. 2010;30:325-330.

[7] Fang, Z. Tang B. Si F, et al. Temperature stable and high-Q microwave dielectric ceramics in the $Li_2Mg_{3-x}Ca_xTiO_6$ system (x=0.00–0.18). *Ceram. Int*. 2017;43:1682-1687.

[8] Bi, JX. Li CC. Zhang YH, et al. Crystal structure, infrared spectra and microwave dielectric properties of ultra low-loss $Li_2Mg_4TiO_7$ ceramics. *Mater. Lett*. 2017;196:128-131.

[9] Wu, H. Kim ES. Correlations between crystal structure and dielectric properties of high-Q materials in rock-salt structure Li_2O–MgO–BO_2 (B= Ti, Sn, Zr) systems at microwave frequency. *RSC. Adv*. 2016;6:47443-47453.

[10] Fu, Z. Liu P. Ma J, et al. Novel series of ultra-low loss microwave dielectric ceramics: $Li_2Mg_3BO_6$ (B = Ti, Sn, Zr). *J. Eur. Ceram. Soc*. 2016;36:625-629.

[11] Bian, JJ. Dong YF. Sintering behavior, microstructure and microwave dielectric properties of $Li_{2+x}TiO_3$ ($0 \le x \le 0.2$). *Mater. Sci. Eng. B*. 2011;176:147-151.

[12] Xu, N-X. Zhou J-H. Yang H, et al. Structural evolution and microwave dielectric properties of MgO–LiF

co-doped Li_2TiO_3 ceramics for LTCC applications. *Ceram. Int*. 2014;40:15191-15198.

[13] Zhou, H. Tan X. Huang J, et al. Phase structure, sintering behavior and adjustable microwave dielectric properties of $Mg_{1-x}Li_{2x}Ti_xO_{1+2x}$ solid solution ceramics. *J. Alloy. Compd*. 2017;696:1255-1259.

[14] Castellanos, M. West AR. Compound and solid solution formation in the system, Li_2SnO_3-MgO. *J. Mater. Sci. Lett*. 1984;3:786-788.

[15] Fu, Z. Liu P. Ma J, et al. Microwave dielectric properties of low-fired Li_2SnO_3 ceramics co-doped with MgO–LiF. *Mater. Res. Bull*. 2016;77:78-83.

[16] van Keulen, ANJ. Hoogendam GC. Seshan K, et al. The role of tin in Li/Sn/MgO catalysts for the oxidative coupling of methane. *J. Chem. Soc., Chem. Commun*. 1992;1546-1547.

[17] Liu, CT. Loh BTM. Solid-solution theory and spinodal decomposition. *Philos. Mag*. 1971;24:367-380.

[18] Shannon, Rt. Revised effective ionic radii and systematic studies of interatomic distances in halides and chalcogenides. *Acta Crystallogr. Sect. A*. 1976;32:751-767.

[19] Iida, Y. Evaporation of Lithium Oxide from Solid Solution of Lithium Oxide in Nickel Oxide. *J. Am. Ceram. Soc*. 1960;43:171-172.

[20] Momma, K. Izumi F. VESTA 3 for three-dimensional visualization of crystal, volumetric and morphology data. *J. Appl. Crystallogr.* 2011;44:1272-1276.

[21] Huang, SG. Li L. Vanmeensel K, et al. VC, Cr_3C_2 and NbC doped WC–Co cemented carbides prepared by pulsed electric current sintering. *Int. J. Reefract. Met. H*. 2007;25:417-422.

[22] Hauck, J. Short-range order and superstructures of ternary oxides AMO_2, A_2MO_3 and A_5MO_6 of monovalent A and multivalent M metals related to the NaCl structure. *Acta Crystallogr. Sect. A*. 1980;36:228-237.

[23] George, S. Sebastian MT. Microwave dielectric properties of novel temperature stable high Q $Li_2Mg_{1-x}Zn_xTi_3O_8$ and $Li_2A_{1-x}Ca_xTi_3O_8$ (A = Mg, Zn) ceramics. *J. Eur. Ceram. Soc*. 2010;30:2585-2592.

[24] Denisova, TA. Maksimova LG. Polyakov EV, et al. Metatitanic acid: Synthesis and properties. *Russ. J. Inorg. Chem*. 2006;51:691-699.

[25] Liao, Q. Li L. Structural dependence of microwave dielectric properties of ixiolite structured $ZnTiNb_2O_8$ materials: crystal structure refinement and Raman spectra study. *Dalton. T*. 2012;41:6963-6969.

[26] Chen, GH. Yuan CL. Zhou CR, et al. Low-firing high permittivity $Ca_{0.6}Sm_{0.8/3}TiO_3$–$(Li_{0.5}Nd_{0.5})TiO_3$ ceramics with $BaCu(B_2O_5)$ addition. *Ceram. Int*. 2013;39:9763-9766.

[27] Fang, ZX. Tang B. Li E, et al. High-Q microwave dielectric properties in the $Na_{0.5}Sm_{0.5}TiO_3$ + Cr_2O_3 ceramics by one synthetic process. *J. Alloy. Compd*. 2017;705:456-461.

[28] Zhao, Y. Zhang P. High-Q microwave dielectric ceramics using $Zn_3Nb_{1.88}Ta_{0.12}O_8$ solid solutions. *J. Alloy. Compd*. 2016;662:455-460.

[29] Kim, ES. Kim SH. Yoon KH. Dependence of Thermal Stability on Octahedral Distortion of (1-x)$(Ca_{0.3}Li_{0.119}Sm_{0.427})TiO_{3-x}$-$LnAlO_3$ (Ln=Nd, Sm) Ceramics. *J. Ceram. Soc. Jpn*. 2004;112:S1645-S1649.

[30] Chen, MY. Chia CT. Lin IN, et al. Microwave properties of $Ba(Mg_{1/3}Ta_{2/3})O_3$, $Ba(Mg_{1/3}Nb_{2/3})O_3$ and $Ba(Co_{1/3}Nb_{2/3})O_3$ ceramics revealed by Raman scattering. *J. Eur. Ceram. Soc*. 2006;26:1965-1968.

[31] George, S. Sebastian MT. Synthesis and Microwave Dielectric Properties of Novel Temperature Stable High Q, $Li_2ATi_3O_8$ (A=Mg, Zn) Ceramics. *J. Am. Ceram. Soc*. 2010;93:2164-2166.

[32] Yu, S. Tang B. Zhang S, et al. Temperature stable high-Q microwave dielectric ceramics in $(1-x)BaTi_4O_9$–$xBaZn_2Ti_4O_{11}$ system. *Mater. Lett*. 2012;67:293-295.

[33] Webb, SJ. Breeze J. Scott RI, et al. Raman Spectroscopic Study of Gallium-Doped $Ba(Zn_{1/3}Ta_{2/3})O_3$. *J. Am. Ceram. Soc*. 2002;85:1753-1756.

[34] Dias, A. Khalam LA. Sebastian MT, et al. Chemical Substitution in $Ba(RE_{1/2}Nb_{1/2})O_3$ (RE = La, Nd, Sm, Gd, Tb, and Y) Microwave Ceramics and Its Influence on the Crystal Structure and Phonon Modes. *Chem. Mater.*

2006;18:214-220.

[35]Penn, SJ. Alford NM. Templeton A, et al. Effect of Porosity and Grain Size on the Microwave Dielectric Properties of Sintered Alumina. *J. Am. Ceram. Soc*. 1997;80:1885-1888.

[36]Zhou, D. Randall CA. Wang H, et al. Microwave Dielectric Ceramics in Li_2O–Bi_2O_3–MoO_3 System with Ultra-Low Sintering Temperatures. *J. Am. Ceram. Soc*. 2010;93:1096-1100.

[37]Kim, ES. Kang DH. Yang JM, et al., Crystal Structure and Dielectric Properties of $Ca_{0.85}Nd_{0.1}TiO_3$-$LnAlO_3$ (Ln = Sm, Gd, Dy, Er) Ceramics, in: Applications of Ferroelectrics, 2007. ISAF 2007. Sixteenth IEEE International Symposium on, 2007, pp. 523-524.

[38]Li, J. Han Y. Qiu T, et al. Effect of bond valence on microwave dielectric properties of (1 − x)$CaTiO_3$–x($Li_{0.5}La_{0.5}$)TiO_3 ceramics. *Mater. Res. Bull*. 2012;47:2375-2379.

[39]Ian , MR. Enrico LC. Nava S. Dielectric and Structural Characteristics of Ba- and Sr-based Complex Perovskites as a Function of Tolerance Factor. *Jap. J. Appl. Phys*. 1994;33:3984.

Captions of Figures and Tables

Fig. 1. Schematic representation of the $Li_{2/3(1-x)}Sn_{1/3(1-x)}Mg_xO$ (x=0 to 4/7) placement for providing ZrO_2-burying protective atmosphere and Li-rich sintering atmosphere

Fig. 2. Powder XRD patterns of the $Li_{2/3(1-x)}Sn_{1/3(1-x)}Mg_xO$ ceramic systems (x=0 to 4/7) sintered in controlled atmosphere at optimal temperatures for 5 h

Fig. 3. The representative plots of experimental (red circle) and calculated (blue line) X-ray powder diffraction for the $Li_{2/3(1-x)}Sn_{1/3(1-x)}Mg_xO$ ceramic systems sintered at optimal temperatures for 5 h for (a) x=0, (b) x=1/7, (c) x=1/3 (d) x=2/5 (e) x=1/2 and (f) x=4/7

Fig. 4. The representative schematic illustration of $Li_{2/3(1-x)}Sn_{1/3(1-x)}Mg_xO$ ceramics with typical rock-salt structure for (a) monoclinic structure in C2/c space group (x=0) and (b) cubic structure in Fm-3m space group (x=1/2)

Fig. 5. (a) Raman spectra of $Li_{2/3(1-x)}Sn_{1/3(1-x)}Mg_xO$ ceramic systems sintered at optimal temperatures in controlled atmosphere for 5 h, (b) the amplified spectra of Raman shift around 600 cm^{-1}

Fig. 6. SEM images of $Li_{2/3(1-x)}Sn_{1/3(1-x)}Mg_xO$ ceramic systems sintered at optimal temperatures for 5 h in controlled atmosphere with (a) x=0, (b) x=1/7, (c) x=1/5, (d) x=1/4 (e) x=1/3 (f) x=2/5 (g) x=5/11 (h) x=1/2 and (i) x=4/7

Fig. 7. The representative EDX spectrum of marked grains corresponding to Fig. 6

Fig. 8. Relative density of LSMxO (x=0, 1/7, and 1/3~4/7) sintered at 1200~1400 °C by controlled atmosphere for 5 h

Fig. 9. (a) Dielectric constant of LSMxO (x=0~4/7) sintered at 1200~1400 °C by controlled atmosphere for 5 h, (b) variation of α_m (top right inset), ε_{theo} and ε_r versus the x value, and (c) variation of Raman shift and ε_r versus the x value in the region of 1/3~4/7

Fig. 10. (a) Quality factor of LSMxO (x=0~4/7) sintered at 1200~1400 °C by controlled atmosphere for 5 h, (b) function of FWHM and optimal $Q\times f$ versus the x value, and (c) variation of average grain size and $Q\times f$ versus the x value in the region of 1/3~4/7

Fig. 11. (a) Temperature coefficient of the resonant frequency (τ_f) of LSMxO (x=0~4/7) sintered by controlled atmosphere at optimal temperatures for 5 h, (b) function of octahedral distortion and τ_f versus the x value and (c) variation of $V_{Li/Mg/Sn\text{-}O}$ and τ_f versus the x value in the region of 1/3~4/7

Table 1. Phase composition, crystal structure, lattice parameters, and unit cell volume of $Li_{2/3(1-x)}Sn_{1/3(1-x)}Mg_xO$ systems (x=0 to 4/7) ceramics sintered at optimal temperature by controlled atmosphere

Table 2. The EDX data of $Li_{2/3(1-x)}Sn_{1/3(1-x)}Mg_xO$ ceramics marked grains corresponding to Fig. 6.

Table 3. The bond valence (V_{bv}), octahedral distortion (δ) and packing fraction $Li_{2/3(1-x)}Sn_{1/3(1-x)}Mg_xO$ systems for $1/3 \leq x \leq 1/7$

Table 4. The theoretical dielectric polarizability (α_m), theoretical dielectric constant (ε_{theo}) and observed (ε_r) of $Li_{2/3(1-x)}Sn_{1/3(1-x)}Mg_xO$ systems for $1/3 \leq x \leq 1/7$

Table 5. The exact peak position and corresponding FWHM of Raman spectra at around 643 cm^{-1} versus Cell volume (V), optimal $Q \times f$ and average grain sizes for $Li_{2/3(1-x)}Sn_{1/3(1-x)}Mg_xO$ systems sintered at optimal temperature with $1/3 \leq x \leq 1/7$

Table 1. Phase composition, crystal structure, lattice parameters, and unit cell volume of $Li_{2/3(1-x)}Sn_{1/3(1-x)}Mg_xO$ systems (x=0 to 4/7) ceramics sintered at optimal temperature by controlled atmosphere

$Li_{2/3(1-x)}Sn_{1/3(1-x)}Mg_xO$	Phase and structure		Lattice parameters (Å)			Cell volume V(Å^3)	Reliability factors		
	Phase	structure	a(Å)	bÅ)	c(Å)		R_{wp} (%)	R_p (%)	χ^2
0	LS	monoclinic	5.28891 (12)	9.187223 (17)	10.02642 (15)	479.5692	3.52	2.60	2.231
1/7	LS+L2M3S		LS(W_1=71.82%)+L2M3S(W_2=28.18%)				6.47	5.56	1.89
1/5	LS+L4MS2+L2M3S		Mixture				--	--	--
1/4	LS+L4MS2+L2M3S		Mixture				--	--	--
1/3	L2M3S	cubic	4.25159 (34)	4.25159 (34)	4.25159 (34)	76.852	2.85	1.98	1.295
2/5	L2M3S	cubic	4.24954 (22)	4.24954 (22)	4.24954 (22)	76.740	2.85	1.68	1.531
5/11	L2M3S	cubic	4.24588 (28)	4.24588 (28)	4.24588 (28)	76.542	3.93	2.46	1.755
1/2	L2M3S	cubic	4.24327 (8)	4.24327 (8)	4.24327 (8)	76.401	2.56	1.98	1.614
4/7	L2M3S	cubic	4.23728 (36)	4.23728 (36)	4.23728 (36)	76.079	2.22	1.18	1.827

a, b, c, unit cell parameters; V-cell volume; M- weight fraction ；R_{wp}-reliability factor of weighted patterns, R_p- reliability factor of patterns, χ^2-goodness of fit indicator; W_1-weight fraction of LS phase, W_2-weight fraction of L2M3S phase

Table 2. The EDX data of $Li_{2/3(1-x)}Sn_{1/3(1-x)}Mg_xO$ ceramics marked grains corresponding to Fig. 6.

Spot	Atom (%)			
	Mg	Sn	O	Mg: Sn
A	--	32.83	67.17	0
B	33.05	11.67	55.28	2.83: 1
C	--	30.10	69.90	0
D	7.19	14.98	77.83	0.48: 1
E	34.08	12.11	53.81	2.82: 1
F	8.23	19.98	71.79	0.41: 1
G	33.56	11.23	55.21	2.99: 1
H	26.43	17.16	56.41	1.54:1
I	27.92	14.19	57.89	1.97: 1

J	33.91	13.46	52.63	2.52: 1
K	39.41	12.70	47.89	3.10: 1
L	53.24	13.76	32.99	3.87: 1

Table 3. The bond valence (V_{bv}), octahedral distortion (δ) and packing fraction $Li_{2/3(1-x)}Sn_{1/3(1-x)}Mg_xO$ systems for 1/3 ≤x ≤1/7

Composition	Bond type	d_{ij} (Å)	R_{ij} (Å)	δ (10^{-4})	$V_{Li, Mg, Sn-O}$	Packing fraction (%)
	Li-O	2.12579	1.466	0.00198	1.009	
1/3	Mg-O	2.12579	1.693	0.00198	1.863	39.93
	Sn-O	2.12579	1.905	0.00198	3.304	
	Li-O	2.12477	1.466	0.00203	1.012	
2/5	Mg-O	2.12477	1.693	0.00203	1.868	43.98
	Sn-O	2.12477	1.905	0.00203	3.312	
	Li-O	2.12294	1.466	0.00264	1.016	
5/11	Mg-O	2.12294	1.693	0.00264	1.877	48.94
	Sn-O	2.12294	1.905	0.00264	3.329	
	Li-O	2.12163	1.466	0.00331	1.020	
1/2	Mg-O	2.12163	1.693	0.00331	1.884	53.47
	Sn-O	2.12163	1.905	0.00331	3.341	
	Li-O	2.11864	1.466	0.00425	1.028	
4/7	Mg-O	2.11864	1.693	0.00425	1.899	62.63
	Sn-O	2.11864	1.905	0.00425	3.368	

d_{ij}-length of a bond; R_{ij}- bond valence parameters; δ-octahedral distortion; $V_{Li, Mg, Sn-O}$-bond valence for Li-O, Mg-O and Sn-O

Table 4. The theoretical dielectric polarizability (α_m), theoretical dielectric constant (ε_{theo}) and observed (ε_r) of $Li_{2/3(1-x)}Sn_{1/3(1-x)}Mg_xO$ systems for 1/3 ≤x ≤1/7

x	α_m (Å^3)	ε_{theo}	ε_r	100x(ε_r-ε_{theo})/ε_r
1/3	3.612	12.11652	14.38	15.7405
2/5	3.5838	11.79153	13.72	14.0559
5/11	3.560727	11.60227	12.93	10.2686
1/2	3.5415	11.43307	12.4	7.7979
4/7	3.511286	11.23355	11.56	2.8239

Table 5. The exact peak position and corresponding FWHM of Raman spectra at around 643 cm^{-1} versus Cell volume (V), optimal $Q\times f$ and average grain sizes for

$Li_{2/3(1-x)}Sn_{1/3(1-x)}Mg_xO$ systems sintered at optimal temperature with $1/3 \leq x \leq 1/7$

x	1/3	2/5	5/11	1/2	4/7
Peak position (cm^{-1})	641.7	642.9	643.4	644.173	647.44
V ($Å^3$)	76.852	76.740	76.542	76.401	76.079
FWHM (cm^{-1})	39.06	38.56	37.47	36.22	40.76
$Q \times f$ (GHz)	105,084	110,717	141,685	168,443	125,864
Average grain sizes (um)	5.313	5.844	7.869	9.126	6.148

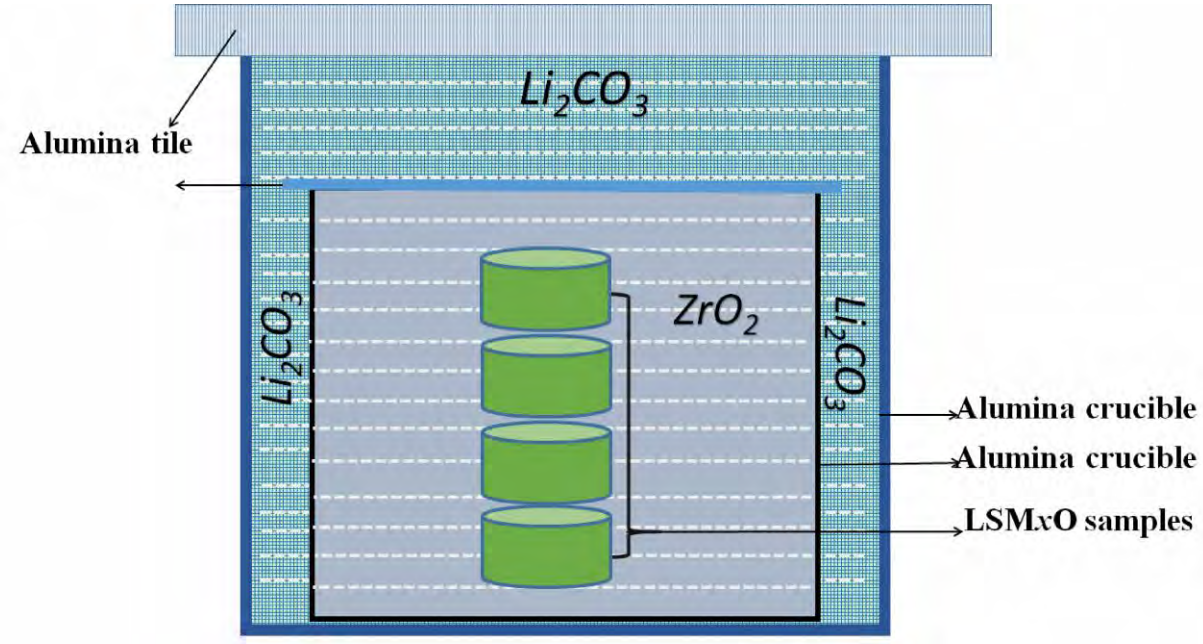

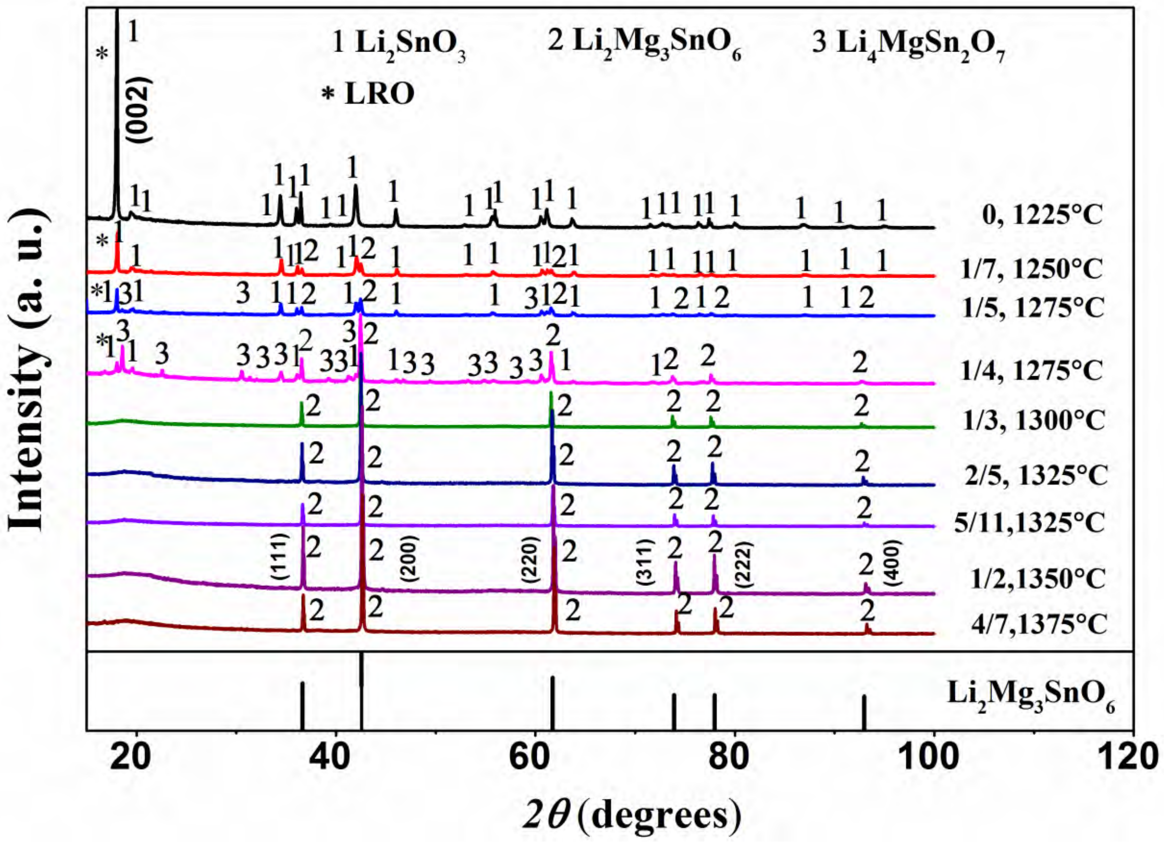
1 Li2SnO3
2 Li2Mg3SnO6
3 Li4MgSn2O7
* LRO
(002)
(111)
(200)
(220)
(311)
(222)
(400)
0, 1225°C
1/7, 1250°C
1/5, 1275°C
1/4, 1275°C
1/3, 1300°C
2/5, 1325°C
5/11,1325°C
1/2,1350°C
4/7,1375°C
Li2Mg3SnO6
Intensity (a. u.)
2θ (degrees)
20
40
60
80
100
120

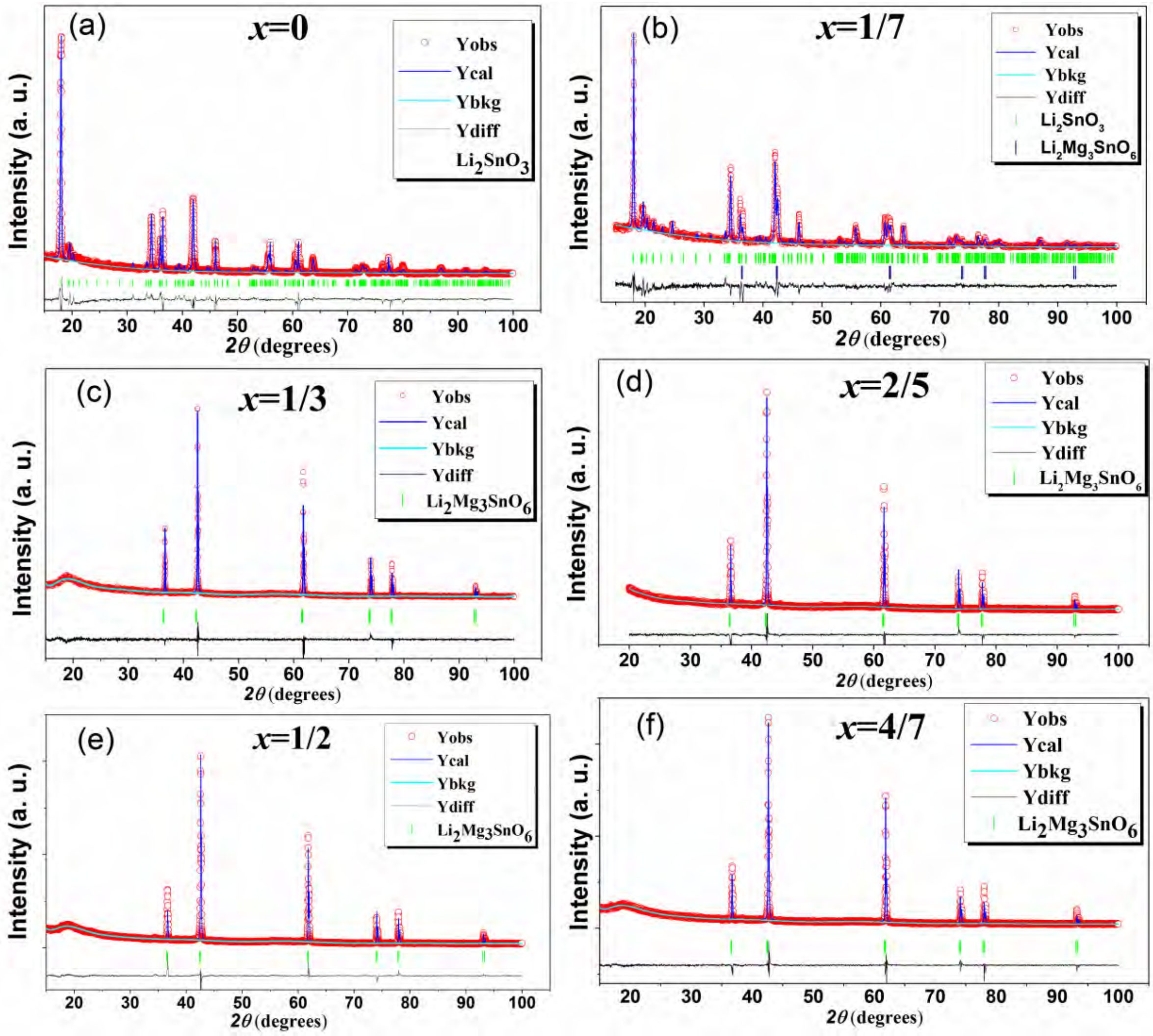
(a)
x=0
Yobs
Ycal
Ybkg
Ydiff
Li2SnO3
(b)
x=1/7
Yobs
Ycal
Ybkg
Ydiff
Li2SnO3
Li2Mg3SnO6
(c)
x=1/3
Yobs
Ycal
Ybkg
Ydiff
Li2Mg3SnO6
(d)
x=2/5
Yobs
Ycal
Ybkg
Ydiff
Li2Mg3SnO6
(e)
x=1/2
Yobs
Ycal
Ybkg
Ydiff
Li2Mg3SnO6
(f)
x=4/7
Yobs
Ycal
Ybkg
Ydiff
Li2Mg3SnO6
Intensity (a. u.)
2θ (degrees)
20
30
40
50
60
70
80
90
100

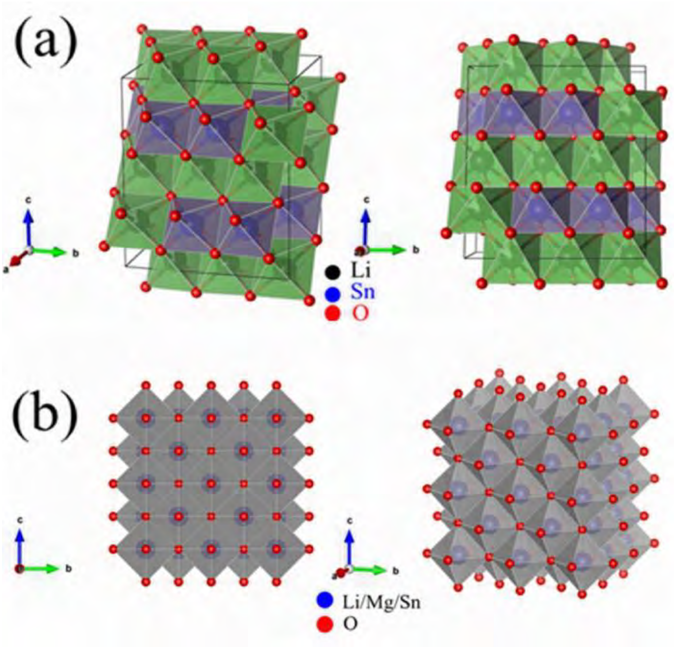
(a)
c
b
a
Li
Sn
O
(b)
c
b
Li/Mg/Sn
O

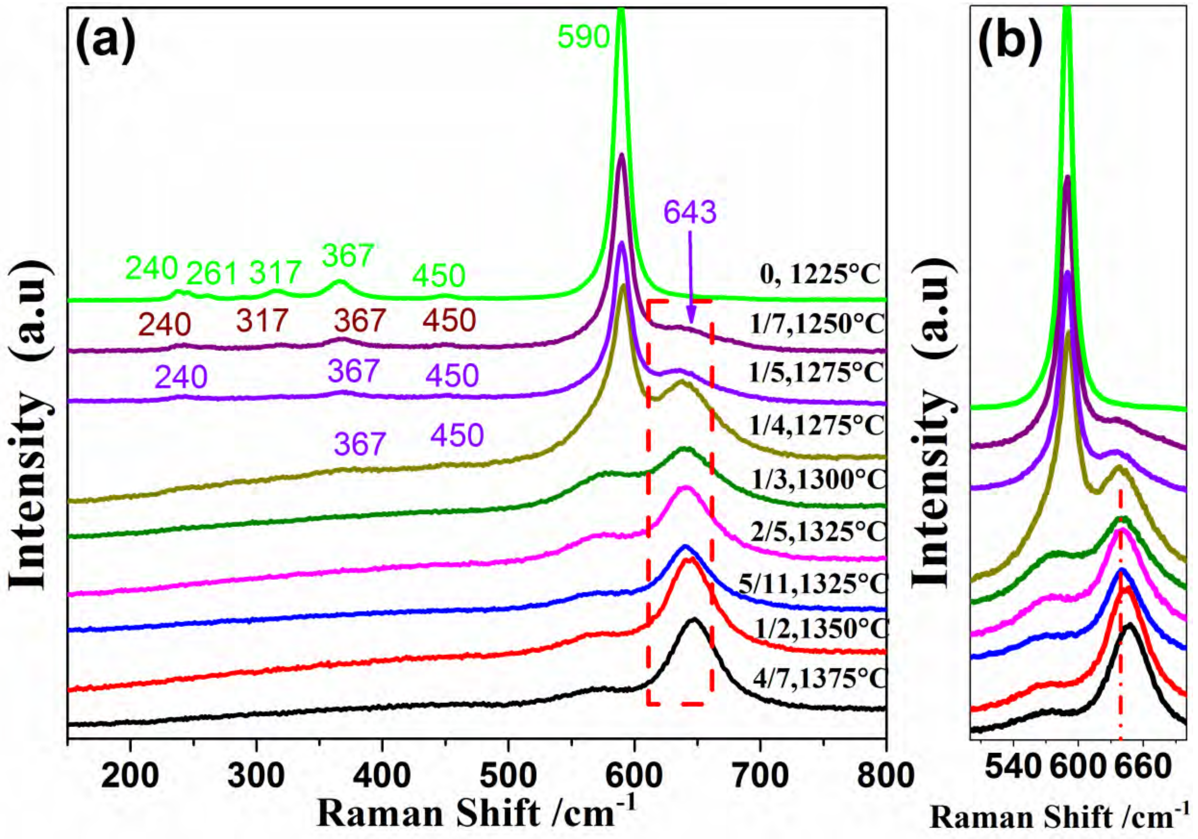
(a)
590
643
240
261
317
367
450
240
317
367
450
240
367
450
367
450
0, 1225°C
1/7,1250°C
1/5,1275°C
1/4,1275°C
1/3,1300°C
2/5,1325°C
5/11,1325°C
1/2,1350°C
4/7,1375°C
Intensity (a.u)
200
300
400
500
600
700
800
Raman Shift /cm-1
(b)
Intensity (a.u)
540
600
660
Raman Shift /cm-1

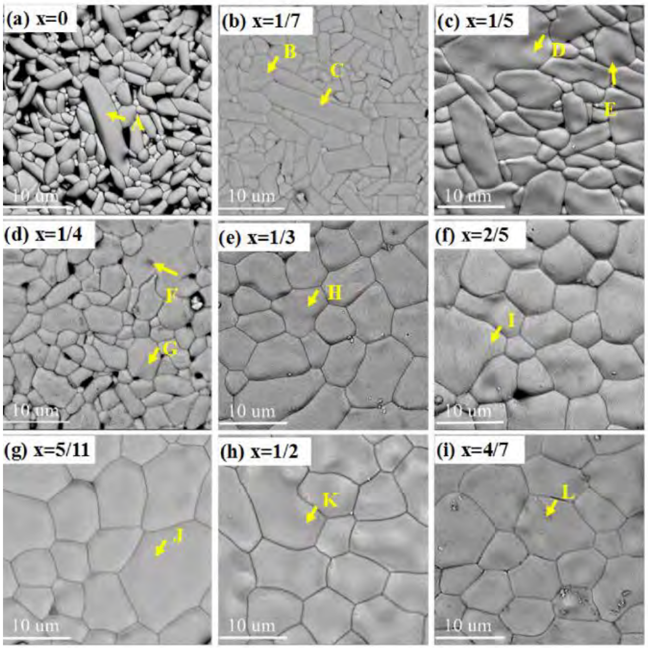
(a) x=0
A
10 um
(b) x=1/7
B
C
10 um
(c) x=1/5
D
E
10 um
(d) x=1/4
F
G
10 um
(e) x=1/3
H
10 um
(f) x=2/5
I
10 um
(g) x=5/11
J
10 um
(h) x=1/2
K
10 um
(i) x=4/7
L
10 um

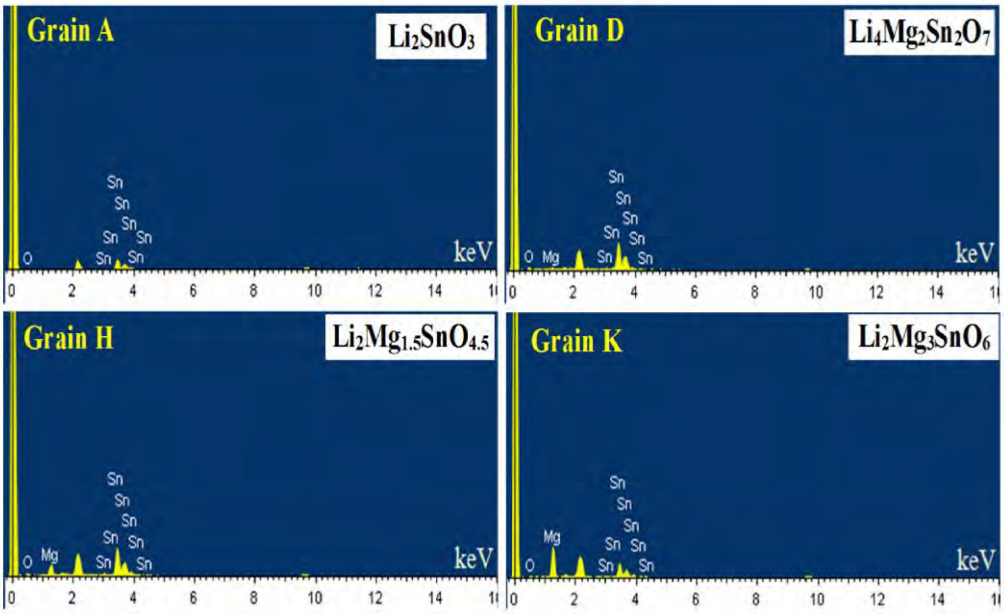
Grain A
Li2SnO3
Grain D
Li4Mg2Sn2O7
Grain H
Li2Mg1.5SnO4.5
Grain K
Li2Mg3SnO6
O
Mg
Sn
keV
0
2
4
6
8
10
12
14

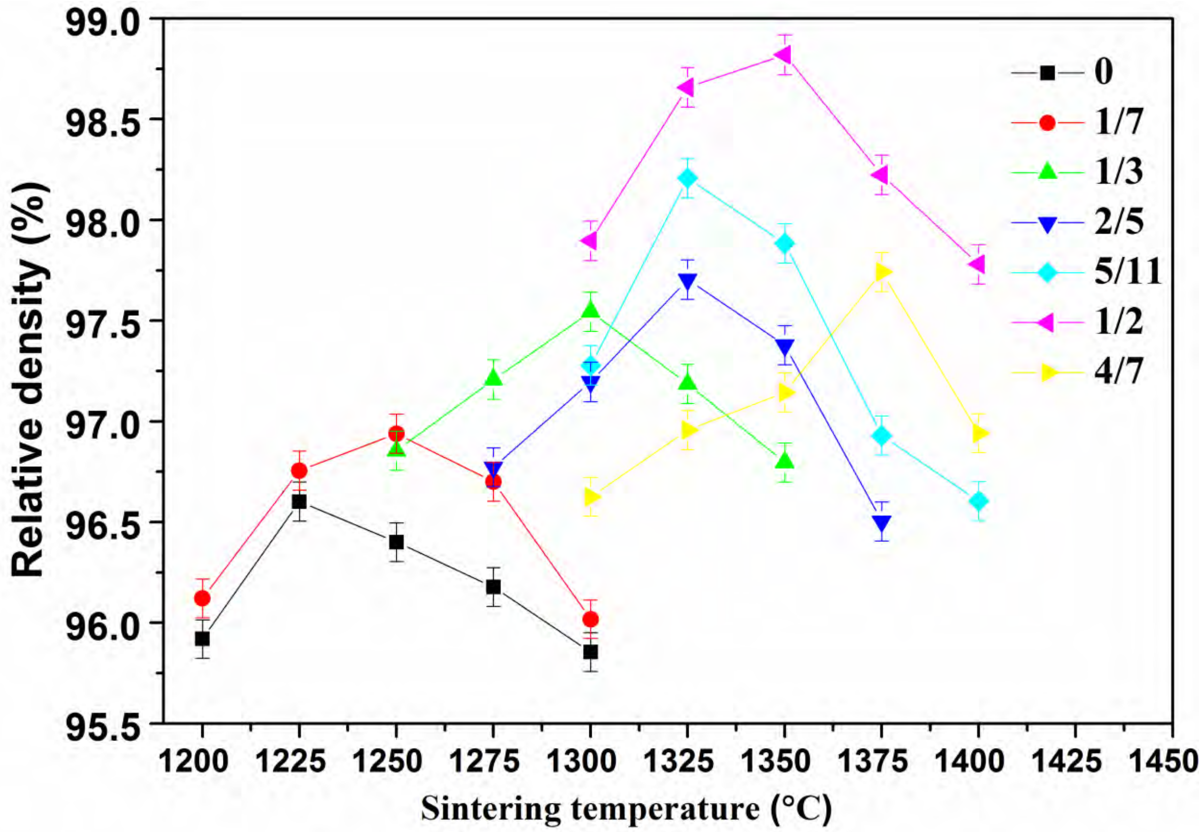
Relative density (%)
Sintering temperature (°C)
99.0
98.5
98.0
97.5
97.0
96.5
96.0
95.5
1200
1225
1250
1275
1300
1325
1350
1375
1400
1425
1450
0
1/7
1/3
2/5
5/11
1/2
4/7

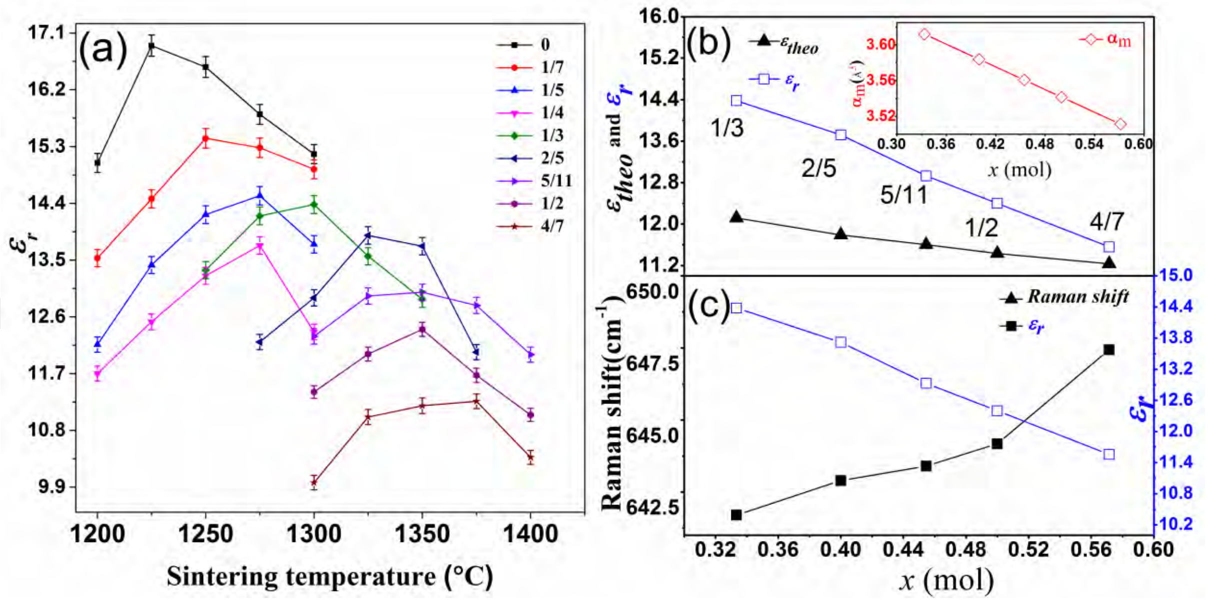
(a)
ε_r
Sintering temperature (°C)
17.1
16.2
15.3
14.4
13.5
12.6
11.7
10.8
9.9
1200
1250
1300
1350
1400
0
1/7
1/5
1/4
1/3
2/5
5/11
1/2
4/7
(b)
ε_{theo} and ε_r
ε_{theo}
ε_r
16.0
15.2
14.4
13.6
12.8
12.0
11.2
1/3
2/5
5/11
1/2
4/7
α_m(Å³)
α_m
3.60
3.56
3.52
0.30
0.36
0.42
0.48
0.54
0.60
x (mol)
(c)
Raman shift(cm⁻¹)
Raman shift
ε_r
650.0
647.5
645.0
642.5
15.0
14.4
13.8
13.2
12.6
12.0
11.4
10.8
10.2
0.32
0.36
0.40
0.44
0.48
0.52
0.56
0.60
x (mol)

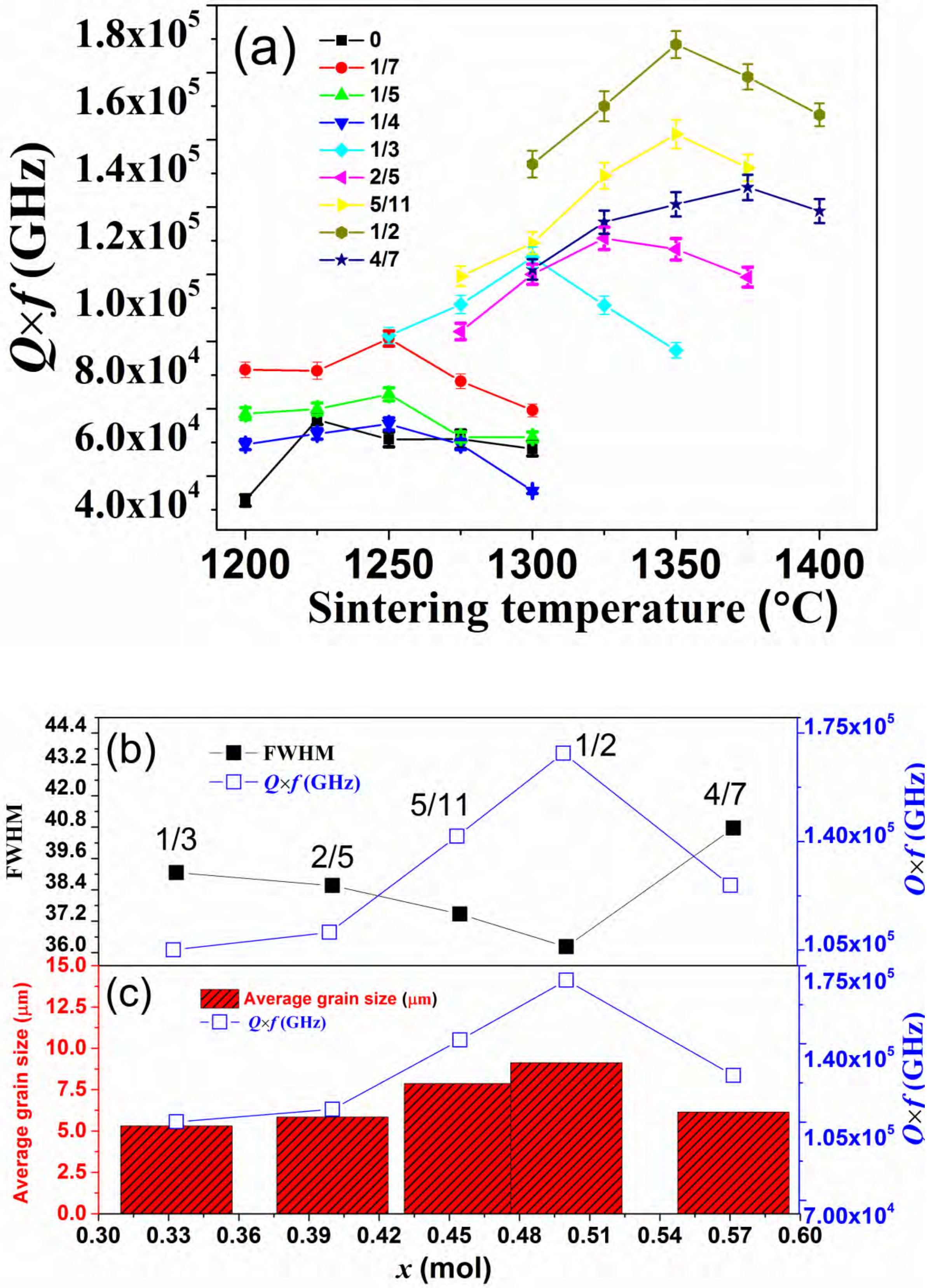
(a)
0
1/7
1/5
1/4
1/3
2/5
5/11
1/2
4/7
Q×f (GHz)
1.8x10^5
1.6x10^5
1.4x10^5
1.2x10^5
1.0x10^5
8.0x10^4
6.0x10^4
4.0x10^4
1200
1250
1300
1350
1400
Sintering temperature (°C)
(b)
FWHM
Q×f (GHz)
1/3
2/5
5/11
1/2
4/7
44.4
43.2
42.0
40.8
39.6
38.4
37.2
36.0
1.75x10^5
1.40x10^5
1.05x10^5
(c)
Average grain size (μm)
Q×f (GHz)
15.0
12.5
10.0
7.5
5.0
2.5
0.0
1.75x10^5
1.40x10^5
1.05x10^5
7.00x10^4
0.30
0.33
0.36
0.39
0.42
0.45
0.48
0.51
0.54
0.57
0.60
x (mol)

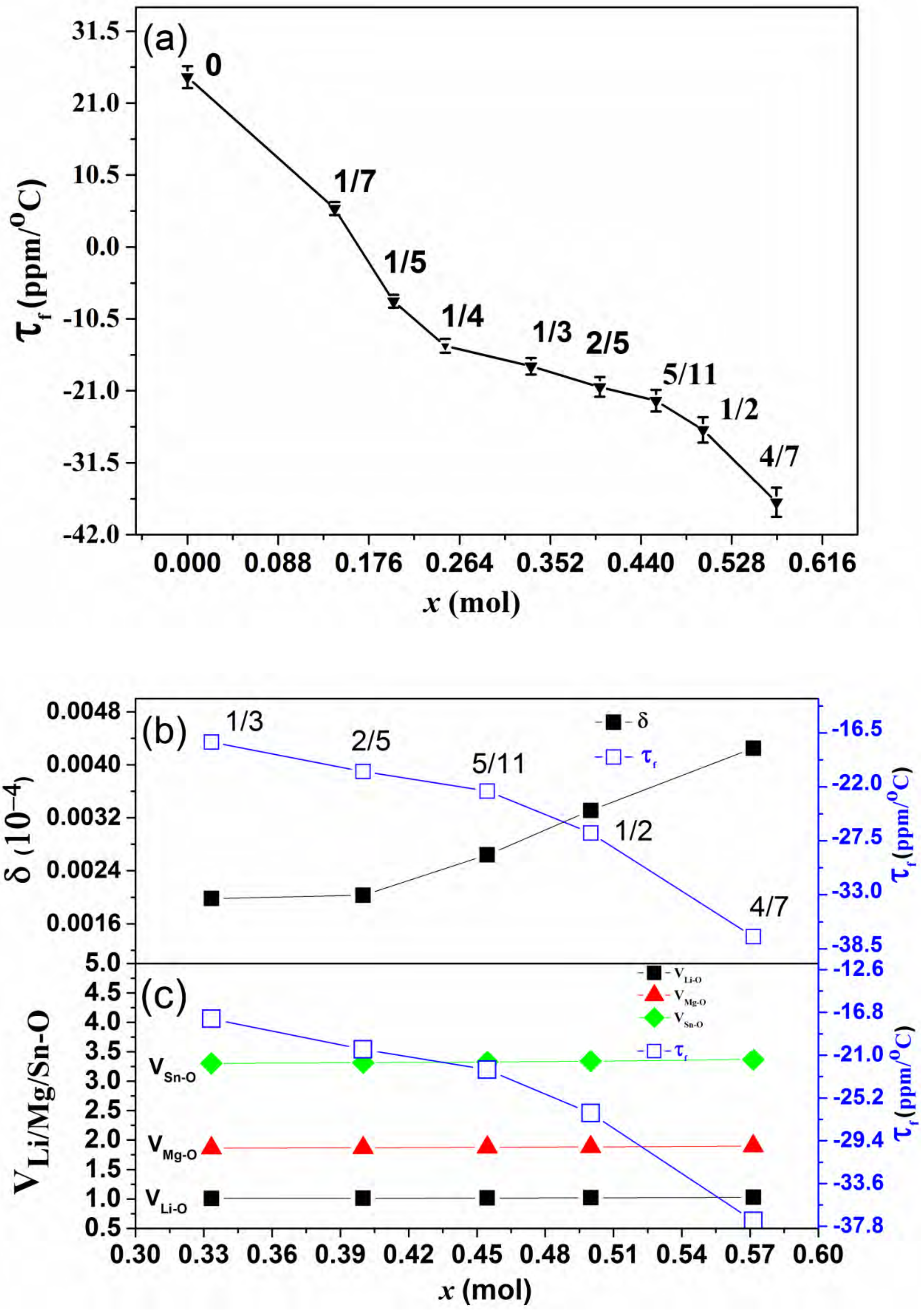
(a)
τf (ppm/°C)
31.5
21.0
10.5
0.0
-10.5
-21.0
-31.5
-42.0
0
1/7
1/5
1/4
1/3
2/5
5/11
1/2
4/7
0.000
0.088
0.176
0.264
0.352
0.440
0.528
0.616
x (mol)
(b)
δ (10⁻⁴)
0.0048
0.0040
0.0032
0.0024
0.0016
1/3
2/5
5/11
1/2
4/7
δ
τf
τf (ppm/°C)
-16.5
-22.0
-27.5
-33.0
-38.5
(c)
V Li/Mg/Sn-O
5.0
4.5
4.0
3.5
3.0
2.5
2.0
1.5
1.0
0.5
V Sn-O
V Mg-O
V Li-O
V Li-O
V Mg-O
V Sn-O
τf
τf (ppm/°C)
-12.6
-16.8
-21.0
-25.2
-29.4
-33.6
-37.8
0.30
0.33
0.36
0.39
0.42
0.45
0.48
0.51
0.54
0.57
0.60
x (mol)